Energy Technology
Generation, Conversion, Storage, Distribution
www.entechnol.de

Hydrothermal Carbonization-Derived Carbon from Waste Biomass as Renewable Pt Support for Fuel Cell Applications: Role of Carbon Activation

Dana Schonvogel, Manuel Nowotny, Tim Woriescheck, Hendrik Multhaupt, Peter Wagner, Alexander Dyck, Carsten Agert, and Michael Wark**

Pt catalysts in proton exchange membrane fuel cells (PEMFCs) typically use carbon blacks such as Vulcan (Vulcan is a registered trademark of the company Cabot Corporation) based on fossil sources. Thus, an important research task is using sustainable supports in PEMFCs. Hydrothermal carbonization (HTC) converts biomasses into chars, which are possible substitutes for fossil-based carbons. Herein, a Pt catalyst derived from HTC of coconut shells is developed for catalysis of O_2 reduction in acidic media. Thermal activation enlarges the specific surface area by factor of 7 to 546 $m^2 g^{-1}$ and generates electrical conductivity making the material suitable for catalysis. Pt particles of 1.8 ± 0.5 nm are distributed well on the activated carbon. Cyclic and CO stripping voltammetry show an electrochemical surface area (ECSA) of 69 ± 21 $m^2 g_{Pt}^{-1}$, almost identical to that of the commercial catalyst using Vulcan (69 ± 6 $m^2 g_{Pt}^{-1}$). Although ECSAs are highly comparable, the activity for O_2 reduction is lower compared with the commercial catalyst. HTC-derived carbon has a lower degree of graphitization, less functional oxygen groups on its surface, and a lower electrical conductivity than Vulcan. This suggests different Pt–support interactions.

1. Introduction

The steadily increasing world population[1] results in higher consumption, mobility, and need of energy, which leads to increasing carbon dioxide emission as one of the biggest issues for the present-day mankind.[2] Thus, the Paris agreement from 2015 intends to limit the global average temperature through reduction in greenhouse gas emission.[3] One promising route to achieve this goal is to establish alternatives for petroleum-based products. It is estimated that 118 billion tons of biomass is available each year as dry matter and therefore represents an abundant feedstock.[4] Furthermore, biomasses are potential carbon sinks due to CO_2 binding in plants.[5,6] Especially, the transformation of waste products into high-quality products such as activated carbons has gained high importance during the last years.[7–9] Hydrothermal carbonization (HTC) has advantages compared with other carbonization methods such as pyrolysis[10–12] or hydrothermal liquification.[13–15] HTC takes place in autoclaves at reaction temperatures <300 °C and allows the direct carbonization of wet biomasses (e.g., manure, sewage sludge) without any drying step.[16] The obtained chars are lignite-like products characterized by a high number of functional oxygen groups present on the surface and typically small specific surface areas. They are called hydrochars[17,18] that are used as, e.g., adsorption agents during purification of sewage or exhaust gases.[19–22] Moreover, hydrochars have shown potential for becoming a substitute for petroleum-based electrodes and catalyst support materials in applications such as supercapacitors[23,24] or fuel cells.[25,26]

Therefore, physical, chemical, or thermal activations are reported in several studies to promote the carbonization of hydrochars and to increase the specific surface area. For example, Ledesma et al.[27] added a controlled oxidizing gas stream into the

Dr. D. Schonvogel, P. Wagner, Dr. A. Dyck, Prof. C. Agert
Division Fuel Cells
DLR Institute of Networked Energy Systems
Carl-von-Ossietzky-Str. 15, Oldenburg 26129, Germany
E-mail: dana.schonvogel@dlr.de

The ORCID identification number(s) for the author(s) of this article can be found under https://doi.org/10.1002/ente.201900344.

DOI: 10.1002/ente.201900344

Dr. D. Schonvogel, M. Nowotny, T. Woriescheck, Dr. H. Multhaupt, Prof. M. Wark
Institute of Chemistry
Chemical Technology 1
Carl von Ossietzky University Oldenburg
Carl-von-Ossietzky Str. 9-11, Oldenburg 26129, Germany
E-mail: michael.wark@uni-oldenburg.de

autoclave and achieved a specific surface area of 320 $m^2 g^{-1}$. Post-treatment methods are state of the art and provide activated hydrochars with higher surface areas.[19,28,29] Postactivation can be done by thermal treatments,[30] physical treatment using steam,[31] or chemical treatments using steam with KOH,[32,33] NaOH,[34,35] or H_3PO_4[36] additives. Especially, KOH-activated carbons from biomass can have high specific surface areas of 2000–3000 $m^2 g^{-1}$.[32] Wei et al. reported 2125–2967 $m^2 g^{-1}$ after 1 h at 700–800 °C.[24] The surface areas of carbons activated with phosphoric acid are typically lower compared with those from alkali hydroxides and are of less interest.[36] Thermal treatments of hydrochars at 800–900 °C in different atmospheres were reported to result in an activated carbon with 1190 $m^2 g^{-1}$.[26] Pyrolysis of hydrochars at 900 °C for 4 h in nitrogen atmosphere led to carbons with surfaces areas of 189–321 $m^2 g^{-1}$.[25]

Carbon supports in Pt catalysts, for oxygen reduction reaction (ORR) in proton exchange membrane fuel cells (PEMFC), require a maximized surface area and a defective carbon surface for anchoring and distributing Pt nanoparticles, porosity for mass transport, and electrical conductivity to guarantee the electron transfer to catalytic active Pt sites.[37,38] To this day, carbon blacks such as Vulcan (Nafion is a registered trademark of The Chemours Company FC LLC) based on hydrocarbons from fossil sources are the commonly used support materials. Vulcan XC72 consists of spherically shaped nanoparticles with diameters of around 30 nm and has a specific surface area of around 240 $m^2 g^{-1}$.[39,40]

With respect to sustainable sources in view of Pt supporting in acidic media, some studies have investigated activated carbons obtained from real biomasses. Dhelipan et al.[41] have pyrolyzed H_3PO_4-impregnated orange peels at 600 °C for 24 h to obtain a carbon support with 640 $m^2 g^{-1}$. Their final Pt catalyst resulted in an electrochemical surface area (ECSA) of 18 $m^2 g_{Pt}^{-1}$ and an onset potential for ORR of 0.84 V_{RHE}. Only a few studies have used HTC to synthesize Pt catalyst supports for PEMFC application, but are limited to much simpler chemical compounds compared with more complex biomasses. Sevilla et al.[42] used saccharides for HTC at 180–240 °C followed by nickel nitrate impregnation and pyrolytic activation at 900 °C. They used the activated carbons with 114–134 $m^2 g^{-1}$ for the deposition of Pt nanoparticles and measured an ECSA of 67–85 $m^2 g_{Pt}^{-1}$. In another study, Taleb et al.[26] carried out HTC of D-glucose at 260 °C for 24 h followed by thermal treatment at 800–900 °C in different atmospheres to get carbon particles with 1190 $m^2 g^{-1}$. After Pt deposition, they have measured an ECSA of 23 $m^2 g_{Pt}^{-1}$ and an ORR onset in the potential range of 0.90–0.95 V_{RHE}.

In view of coconut shells as a source in sustainable energy supply, Wang et al.[43] prepared a nitrogen-containing carbon for ORR in alkaline media and activated the char based on the coconut shells at 800 °C in the presence of KOH followed by HNO_3 and NH_3 treatments. They obtained a catalyst with ORR performance comparable with commercial Pt/C and verified the catalysis to follow the $4e^-$ pathway. Borghei et al.[44] prepared N,P-doped carbons from coconut shells via activation through H_3PO_4 at 550 °C followed by urea treatment and pyrolysis at 1000 °C. Their materials showed high surface areas up to 1216 $m^2 g^{-1}$ and catalytic ORR activity in alkaline media comparable with commonly used Pt/C. Against the background of waste utilization, Esfahani et al.[45] used coconut shells to produce H_2-rich syngas. They mixed the shells with polyethylene waste and applied steam gasification followed by tar cracking achieving a carbon conversion efficiency of 92.4 wt%.

The investigation of Pt catalyst supports in an acidic environment obtained from HTC beyond simple chemical compounds such as saccharides has not been reported yet. The more complex waste biomasses such as coconut shells consist of a diversity of organic compounds, which makes the HTC process and the subsequent carbon activation much more complex. This study presents the synthesis and application of a Pt support for ORR through HTC of coconut shells. Apart from identification of the most suitable hydrochar activation in case of fuel cell catalyst supporting, this study further provides the electrochemical verification of the HTC-derived carbon as a renewable Pt support for ORR. In the first part, the hydrochar is activated by three ways in comparison: physical activation ("Phys") using steam at 650 °C, chemical activation ("Chem") using steam with KOH at 650 °C, and last thermal activation ("Pyr") using pyrolysis at 1100 °C. The most suitable activation in case of fuel cell application is identified by physical analyses and comparison with common Vulcan. In the second part, the most suitable carbon is applied for the deposition of Pt nanoparticles and physically analyzed toward Pt distribution. In the third part, the final electrocatalyst is used for ORR within an electrochemical half-cell and compared to a commercial catalyst using common Vulcan.

2. Results and Discussion

2.1. Activation of Hydrochar

Physical characterization methods are used to identify suitable activation of hydrochar for application as catalyst support in fuel cells. To see the effects of activation, untreated char is investigated by the same methods. To further understand the suitability for fuel cell application, commercial carbon black (C) is investigated as well and compared to the activated carbons. Porosity is the criterion for the mass transport inside the catalyst layer, the distribution of Pt particles on the support, and analyzed by nitrogen sorption. Thermogravimetric analysis (TGA) and IR spectroscopy are used to identify functional surface groups. The electrical conductivities are assessed by the four-point probe measurement.

Figure 1 compares TGA curves and their first derivate of the char before activation to curves of the char after different activations. The untreated hydrochar in Figure 1a shows the onset of mass loss at 142 °C and a total loss of 57.1 wt% after heating to 900 °C. The derivate shows overlapped steps of mass loss with the largest step at 427 °C, evidenced by the minimum in the first derivate. The TGA curves of the activated carbons are depicted in Figure 1b. The carbon black has an onset of mass loss at 600 °C. The total loss of mass without any visible step is 3.2 wt%. The samples Phys and Chem resulted in almost identical curves due to comparable conditions during the activation process. The difference between use of deionized water and use of 1 mol L^{-1} KOH is negligible. Both samples show the onset of mass loss at a temperature of 433 °C. Phys lost 15.3 wt% with a distinct step evidenced by the minimum in first derivate at around 695 °C, whereas Chem lost 17.8 wt% with a distinct step at around 665 °C. Furthermore, the sample Pyr lost 9.9 wt% without any visible mass loss step during TGA and is most comparable with carbon

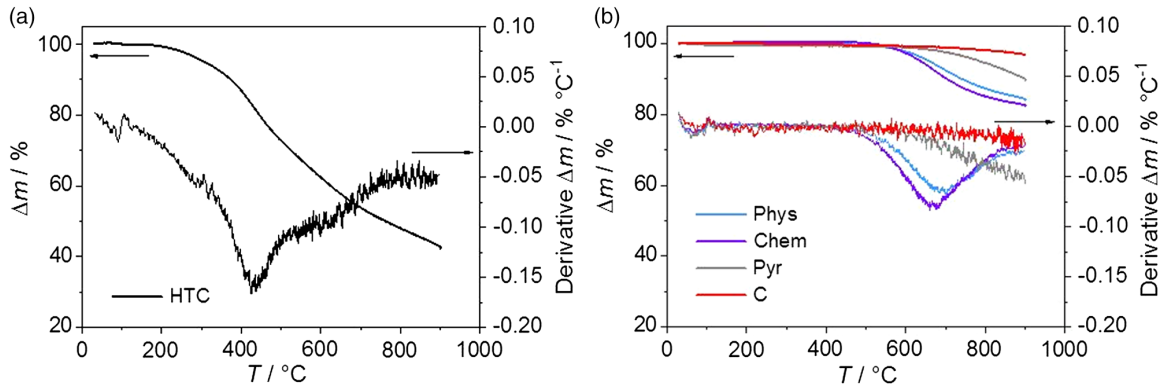

Figure 1. TGA curves with first derivate of mass loss: a) the untreated hydrochar (HTC) and b) the hydrochar after physical, chemical, and thermal activation (Phys, Chem, and Pyr) in comparison with carbon black (C).

black. Thus, the pyrolysis resulted in highest thermal stability of the HTC-derived material, which indicates the highest aromatic carbon content. The lowest mass loss for carbon black is explained by its usual production at temperatures of around 1400–1700 °C.[46] The other carbon materials from this study were treated at lower temperatures as described in the Experimental Section.

Figure 2 compares the IR spectra of the char before and after activations. The hydrochar in Figure 2a exhibits significant absorption of IR radiation at different wavenumbers. A broad and distinct IR absorption band appears at around 3374 cm^{-1} and originates from O–H bond stretching, which is mainly due to residual water. At lower wavenumbers, C=O stretching of carbonyl groups at 1703 cm^{-1} and C=C stretching of aromatic structures at 1604 cm^{-1} are detected. Bands of C–O stretching are visible in the range of 1220–1010 cm^{-1} and result from functional epoxy, ether, or ester groups. In contrast to the hydrochar, the activated carbons in Figure 2b have less IR adsorption bands and thus less functional surface groups. Each sample shows the absence of O–H stretching at around 3374 cm^{-1}, so that each activation results in the removal of hydroxyl groups. With respect to the samples Phys and Chem, residual hydroxyl groups are indicated at around 3700 cm^{-1}. The IR spectra are very similar and still possess C=O stretching at 1703 cm^{-1} and C=C stretching at 1604 cm^{-1}. But, compared with the untreated hydrochar in Figure 2a, the ratio of band intensities changed. This means that after physical and chemical activation, more aromatic structures are present than carbonyl groups, respectively. The activation by pyrolysis led to the largest removal of functional surface groups, which is consistent with the TGA results in Figure 1, and, based on the TGA and IR spectroscopy results, to a carbon mostly similar to carbon black. The thermal annealing of graphitic samples between 700 and 1200 °C was shown in other studies to remove the hydroxyl groups, whereas carbonyl groups are more stable and only removed at temperatures of at least 1200 °C.[47,48] Here, physical and chemical activation is carried out at 650 °C and thermal activation at 1100 °C; hence, hydroxyl groups are expected to be removed and carbonyl groups are expected to remain.

Nitrogen adsorption and desorption isotherms are depicted in **Figure 3**a for original hydrochar and Figure 3c for activated chars and Vulcan. The isotherms are comparable and correspond to type II of International Union of Pure and Applied Chemistry

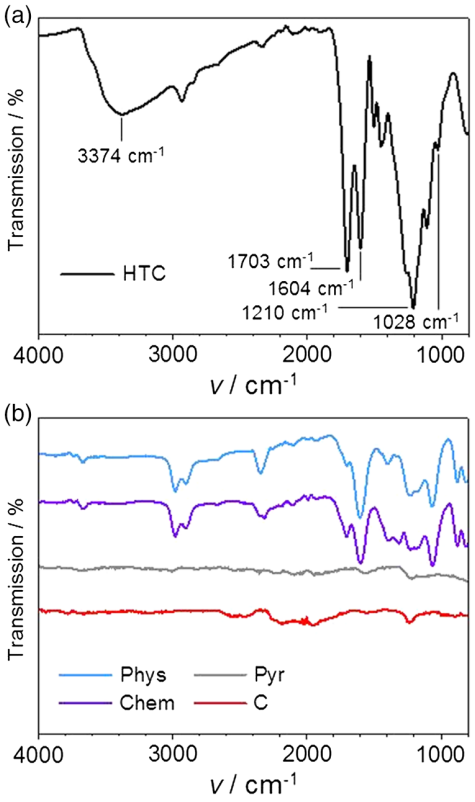

Figure 2. a) IR spectra of the untreated hydrochar (HTC) and b) the hydrochar after physical, chemical, and thermal activation (Phys, Chem, and Pyr) in comparison with carbon black (C).

(IUPAC) classification.[49] Below $p/p_0 = 0.05$, the physisorption of N_2 fills the micropores first followed by a linear regime at $p/p_0 = 0.05$–0.75 related to further N_2 sorption in larger pores. Slopes of the isotherms in the regime $p/p_0 = 0.05$–0.75 are closely between 36–56 $cm^3\ g^{-1}$ and thus verify comparable porosities of original hydrochar, activated carbons, and carbon black. Above $p/p_0 = 0.75$, the adsorbed volumes further increase because of additional N_2 sorption inside pores typically larger than 10 nm in diameter.

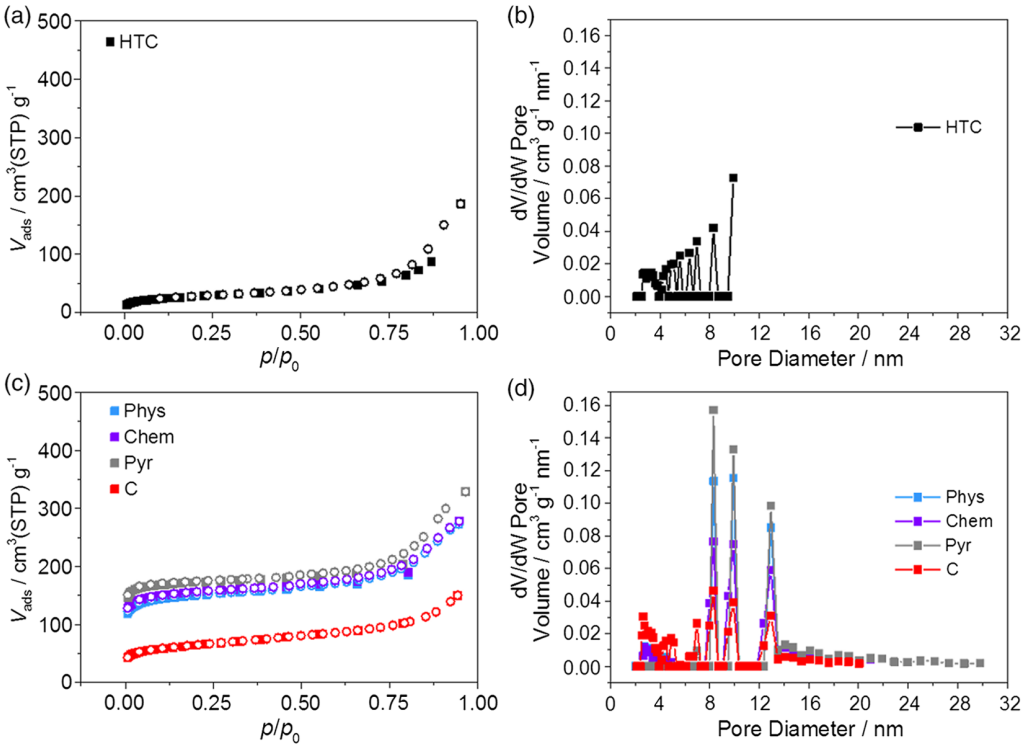

Figure 3. a) Isotherms of nitrogen adsorption (filled squares) and desorption (open circles) of the untreated hydrochar (HTC) with b) pore-size distribution and c) the hydrochar after physical, chemical, and thermal activation (Phys, Chem, and Pyr) in comparison with carbon black (C) with d) pore-size distribution.

Specific surface areas from Brunauer–Emmett–Teller (BET) model are listed in **Table 1**. The char derived from HTC shows by far the lowest area of 79 $m^2 g^{-1}$ followed by carbon black with 218 $m^2 g^{-1}$. In other studies, this carbon black is reported to have 208[39] or 240 $m^2 g^{-1}$.[40] Much larger specific surface areas are achieved by the activation of the hydrochar, which count for Phys 483 $m^2 g^{-1}$, for Chem 499 $m^2 g^{-1}$, and for Pyr 546 $m^2 g^{-1}$. While untreated hydrochars are reported to have very low surface areas below 100 $m^2 g^{-1}$,[16] which is consistent with the char from this study, activations of hydrochar are reported to increase specific surface areas.[26,30–32] Here, the different activations led to an increase by a factor of 6 for physical and chemical activation and a factor of 7 for thermal activation. In other studies, areas after activation using KOH are, e.g., 2125 $m^2 g^{-1}$[24] and after activation using pyrolysis, e.g., 1190,[26] or 189 $m^2 g^{-1}$,[25] which strongly depends on processing parameters during activation and especially on the raw material for HTC. Overall, BET analysis shows first that the porosity of each activated carbon from HTC is comparable to carbon black in terms of forming type II isotherms according to IUPAC classification and second that the specific surface areas of activated chars are much higher than the area of common carbon black.

Table 1. Specific surface areas and electrical sheet resistances of the original char from HTC, the activated carbons (Phys, Chem, and Pyr), and carbon black (C) in comparison.

Sample	Spec. surface area [$m^2 g^{-1}$]	El. sheet resistance [$m\Omega\,\square^{-1}$]
HTC	79	–
Phys	483	40 ± 9
Chem	499	63 ± 12
Pyr	546	22 ± 2
C	218[52,80]	10 ± 2[52,81]

However, a larger surface area based on a larger amount of micropores in the chars has no contribution to the generation of catalytic active centers for ORR, because micropores are not accessible for Pt nanoparticles.[50] Rather, the larger pores are responsible for the porous network of catalyst layers in PEMFCs. Mesopores allow the deposition of Pt nanoparticles on the support surface and the mass transport of reactants to the catalytic active centers.[50] Therefore, besides the calculation of surface areas and IUPAC classification of the isotherm, the distribution of pore sizes is analyzed via density functional theory (DFT) modeling to assess the porosity of the materials. Figure 3b depicts the pore-size distribution of the original char, while Figure 3d compares the activated chars and the carbon black. The pore size of the hydrochar is restricted to 10 nm, whereas the activated chars possess larger pore sizes with a maximum pore volume between 8 and 13 nm. This shows pore enlargement due to the activation processes, which benefits the necessary microstructure of the catalyst layers in the PEM fuel cells. The pores of the untreated hydrochar might be plugged by functional groups, which get lost during the activation processes. Especially,

pyrolysis generates an activated carbon with the largest portion of wider mesopores in comparison. This enlarged mesoporosity improves the suitability for fuel cell catalysis through an enlarged carbon surface for Pt particle deposition. Vulcan in Figure 3d shows a similar pore-size distribution, but a lower pore volume.

Table 1 further compares electrical sheet resistances. Phys and Chem are very comparable with sheet resistances of $40 \pm 9\ m\Omega\,\square^{-1}$ and $63 \pm 12\ m\Omega\,\square^{-1}$, which indicate the similarity of the progress in activation. In case of the untreated char from HTC, the sheet resistance was too high and out of the range for measurement unit. Comparing the activated carbons, Pyr possesses the highest electrical conductivity with a sheet resistance twice as low as the others. The electrical conductivity of Pyr is closest to carbon black. Thus, this activation best generated the electrical conductivity of the char, which is mandatory for catalyst supporting.

In conclusion, HTC char additionally activated by pyrolysis shows the best conditions to present the catalyst support for ORR and is most similar to carbon black as the common Pt support in fuel cells. After thermal activation, the highest values for electrical conductivity and specific surface area and a good porosity are achieved. These factors are usually expected to positively impact the ECSA.[48] Therefore, the carbon material Pyr is further used for deposition of Pt nanoparticles in the next section.

2.2. Physical Catalyst Investigation

Based on the physical analysis (previous section), the sample Pyr is used as a support for deposition of Pt catalyst nanoparticles. Images from transmission electron microscopy (TEM) in **Figure 4** depict the progress in synthesis and compare the hydrochar, the pyrolyzed hydrochar, and the final Pt catalyst. The char in Figure 4a consists of aggregates in nanometer scale with a coherent and undefined network. The heat-treated char in Figure 4b consists of aggregates in similar scale but shows an increased contrast of the sample surface during TEM. This indicates a larger roughness of the carbon surface and a higher surface area and confirms with the results of specific surface areas in Table 1. Furthermore, the loss of material was 56 wt% after pyrolysis. This is highly comparable with the mass loss of hydrochar of 57.1 wt% during TGA in Figure 1a and is traced back to the removal of functional oxygen groups and possible organic compounds or thermally unstable carbon.[51]

The final catalyst Pt/HTC-Pyr is imaged in Figure 4c and consists of Pt nanoparticles on pyrolyzed hydrochar. Pt particles are distributed well on the support, which is caused by van der Waals interaction between platinum particles and the carbon support. Figure 4d shows the size distribution of Pt nanoparticles with an average platinum size of 1.8 ± 0.5 nm. In comparison,

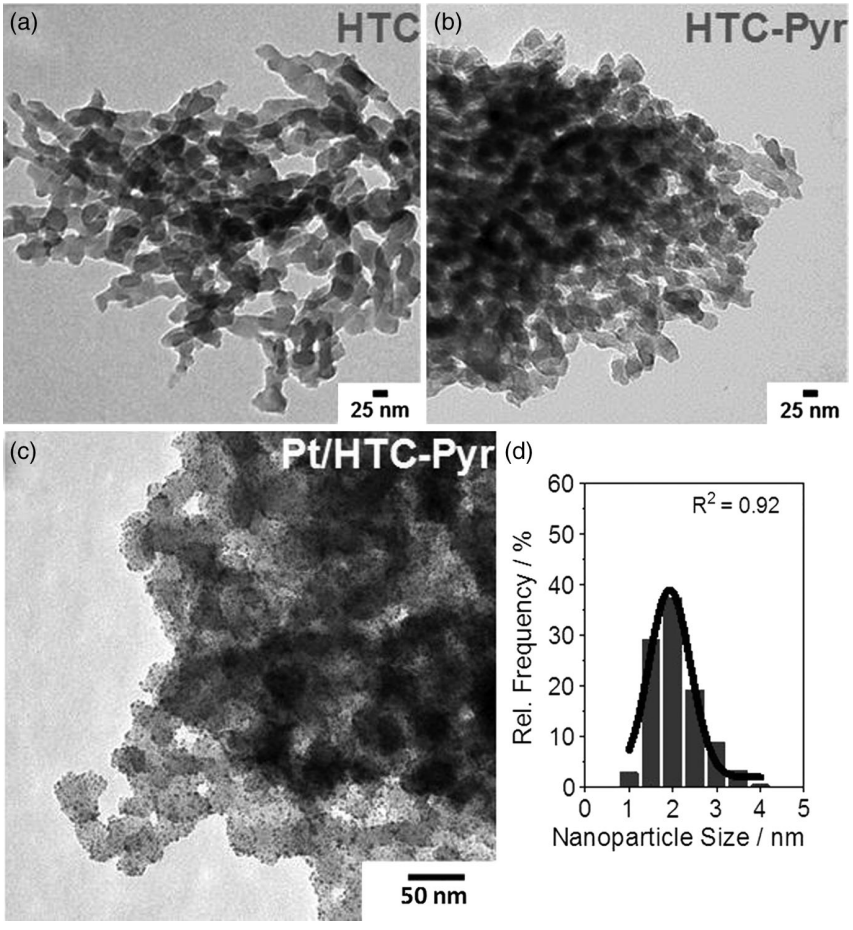

Figure 4. Progress in catalyst synthesis: a) TEM images of original hydrochar (HTC), b) pyrolyzed hydrochar (HTC-Pyr), and c) Pt nanoparticles on pyrolyzed hydrochar (Pt/HTC-Pyr) d) with platinum particle-size distribution.

the commercial Pt/C[52] containing Vulcan also showed well-distributed Pt particles with a Pt size of 1.5 ± 0.4 nm in our previous study. Furthermore, Pt digestion and analysis by inductively coupled plasma MS (ICP-MS) resulted in a Pt loading of 8.3 wt%, which has to be considered in the electrochemical analysis of ECSA and ORR activity later.

Figure 5 shows the X-ray diffraction (XRD) pattern of Pt/HTC-Pyr in comparison with a pattern of standard Pt/C[52] and the reference pattern 00-001-1194 from inorganic crystal structure database (ICSD). The reflections at 40.0° and 46.5° originate from (111) and (200) planes of platinum and overlap due to broad and low-intensity signals. This is caused by Pt nanoparticle sizing, which is also seen in the TEM images of Figure 4. Furthermore, the reflection of (002) plane of graphitic HTC-Pyr is visible at a diffraction angle of 22.7° and corresponds to an interplanar distance of 0.391 nm. This distance is slightly larger than the distance of graphite of ≈0.34 nm[37] and the distance in Vulcan XC72[52] of 0.366 nm. This proves a highly turbostratic graphitic modification of HTC-Pyr.[53] The full width at half maximum (FWHM) counts 5.9°, which is larger than that of Pt on Vulcan XC72[52] counting 2.8°. The Scherrer Equation (1) is used to estimate the crystallite size through the FWHM, the wavelength of Cu Kα radiation λ, the X-ray reflection angle θ, and the cubic form factor K of 0.89. Pt/HTC-Pyr results into a graphitic crystallite size of 1.4 nm, whereas the commercial Pt catalyst[52] has a larger crystallite size of 2.8 nm.

$$\text{Crystallite size} = \frac{K \cdot \lambda}{\text{FWHM} \cdot \cos(\theta)} \quad (1)$$

In conclusion, the Pt nanoparticles show a size of 1.8 ± 0.5 nm, lying in the size range of 1.0–5.0 nm, which is claimed to be the optimum for ORR.[54,55] Particles below 1.0 nm would have a lack in stability, whereas larger particles would reduce the ECSA.[56] Furthermore, both parameters from XRD, the interplanar distance and the crystallite size, indicate a more amorphous structure of HTC-Pyr in comparison with carbon black. On the one hand, this can cause more sites for anchoring of Pt nanoparticles and leads to a good distribution of particles. This is indeed evidenced by TEM in Figure 4 and is expected to positively impact the ECSA.[56] On the other hand, a highly amorphous structure of HTC-Pyr can lead to lowered electrical conductivity compared with carbon black. This is evidenced by Table 1 and might hinder catalytic steps during ORR through electron-transfer barriers between the catalytic active Pt center and its support and, furthermore, can limit the electrochemical stability of the material.[56]

X-ray photoelectron spectroscopy (XPS) results of pyrolyzed hydrochar and carbon black are displayed in **Figure 6** for further comparison of both catalysts. Survey scans in Figure 6a serve for analysis of the main elemental compositions and show carbon

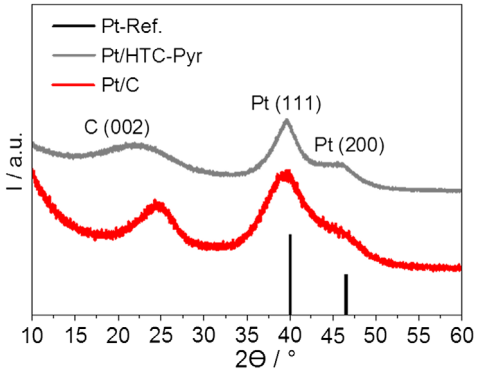

Figure 5. XRD patterns of Pt catalyst using the pyrolyzed hydrochar (Pt/HTC-Pyr) in comparison with Pt/C[52] and Pt reference pattern 00-001-1194 from ICSD.

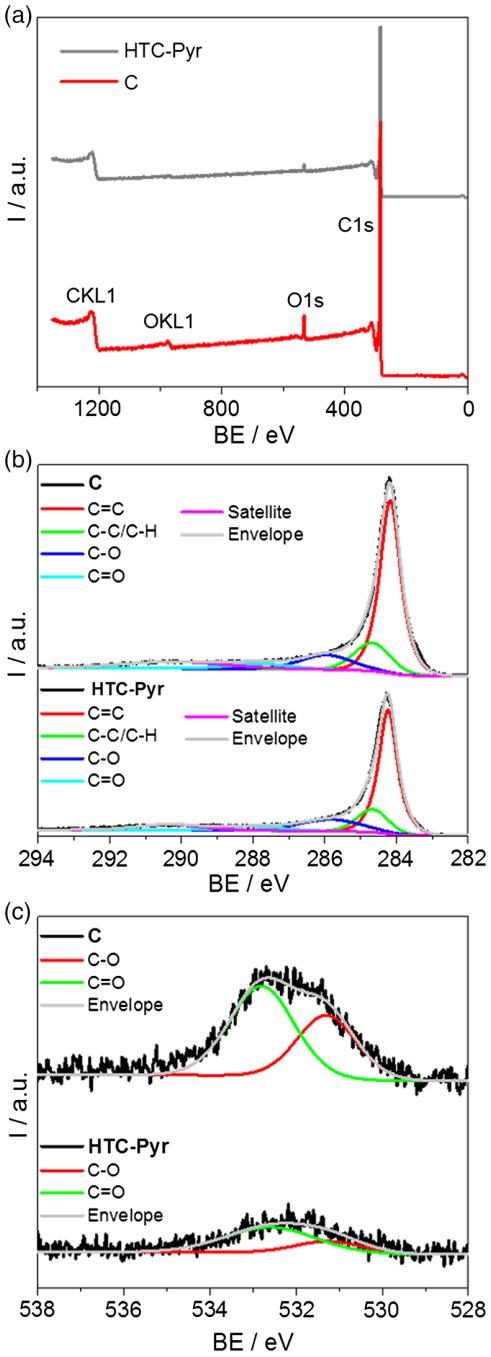

Figure 6. XPS of Pt catalyst using the pyrolyzed hydrochar (HTC-Pyr) in comparison with Vulcan (C): a) survey scans, and b) high-resolution scans of C1s and c) of O1s.

and oxygen. The C/O ratio is derived from the integration and division of C1s and O1s signals counting 24 in case of carbon black and 49 in case of HTC-Pyr. Lower oxygen content of the hydrochar is traced back to the reductive condition of Ar/H_2-atmosphere during pyrolysis. Figure 6b depicts the high-resolution scan of C1s with peak fitting. Both support materials consist of π-bonded carbon from aromatic structures at 284.4 eV as well as σ-bonded carbon at 284.8 eV to a lesser extent. In literature, sp^3-hybridized carbon atoms are located at around 284.8 eV, whereas sp^2-hybridized carbon atoms occur at slightly lower binding energies.[57,58] Next to carbon–carbon bonds, at 285.9 eV, C–O bonds traced back to ether, ester, or epoxy groups, and at 287.9 eV, C═O bonds showing carbonyl groups are detected for both materials.[59] Last, at a binding energy of 290.3 eV, the very broad satellite peak with a low intensity is assigned to π-electron shake-up relaxation through emitted photoelectrons.[57,60] O1s spectra are shown in Figure 6c with a C–O peak centered at 531.0 eV and a C═O peak centered at 532.9 eV for both carbons. The C–O peak intensity is lower, which demonstrates that carbonyl C═O groups occur in higher extent than epoxy, ether, or ester groups on the surfaces of both materials. Overall, XPS reveals larger surface functionalities in terms of oxygen groups for carbon black than for the pyrolyzed hydrochar HTC-Pyr.

2.3. Electrochemical Catalyst Investigation

Pt/HTC-Pyr catalyst, the HTC-Pyr support, and the standard catalyst Pt/C are electrochemically investigated in an analogous way. The cyclic voltammetry (CV) experiments are depicted in **Figure 7**a. CVs of Pt/HTC-Pyr and Pt/C show the typical peaks of hydrogen adsorption and desorption in the potential ranges of 0.00–0.35 V_{RHE}. During the cathodic scans, protons adsorb on the Pt surfaces and get reduced, whereas during the anodic scans, hydrogen atoms get oxidized and desorb. In the potential range of 0.35–0.70 V_{RHE}, the double-layer regions are located, where no electrochemical reactions of platinum are detected. Platinum oxidation and reduction are detected above ≈0.70 V_{RHE}.[61] During anodic scans, Pt hydroxides and further Pt oxides are formed, which get reduced during cathodic scans. The ECSAs are determined via hydrogen underpotential deposition (HUPD) using the hydrogen desorption between 0.00 and 0.35 V_{RHE} and counts 54 $m^2\ g_{Pt}^{-1}$ in case of Pt/HTC-Pyr and 65 $m^2\ g_{Pt}^{-1}$ in case of Pt/C.[52] For calculation using Equation (2), the released charge amount Q_{Pt} during hydrogen desorption is divided by the scan rate υ, the Pt loading m_{Pt} onto the electrode, and the charge density ρ of 2.1 C m_{Pt}^{-2}. Taleb et al.[26] tested an activated carbon derived by HTC of D-glucose with subsequent thermal treatment. They also used HUPD and found a significantly lower ECSA of 23 $m^2\ g_{Pt}^{-1}$, although their specific surface area of the material for Pt supporting was 1190 $m^2\ g^{-1}$ and thus much higher than the material in this study showing 546 $m^2\ g^{-1}$. The reason can be their untypically high Pt loading of 74 wt% in contrast to our Pt loading of 8.3 wt%. A high Pt loading on supports is expected to result in Pt particle aggregation and in consequence in a decreased ECSA.[62] In contrast to the Pt/HTC-Pyr catalyst, for HTC-Pyr support, electrochemical adsorption/desorption of hydrogen and oxygen species are absent, whereas redox activity of hydroquinone/quinone (HQ/Q) similar

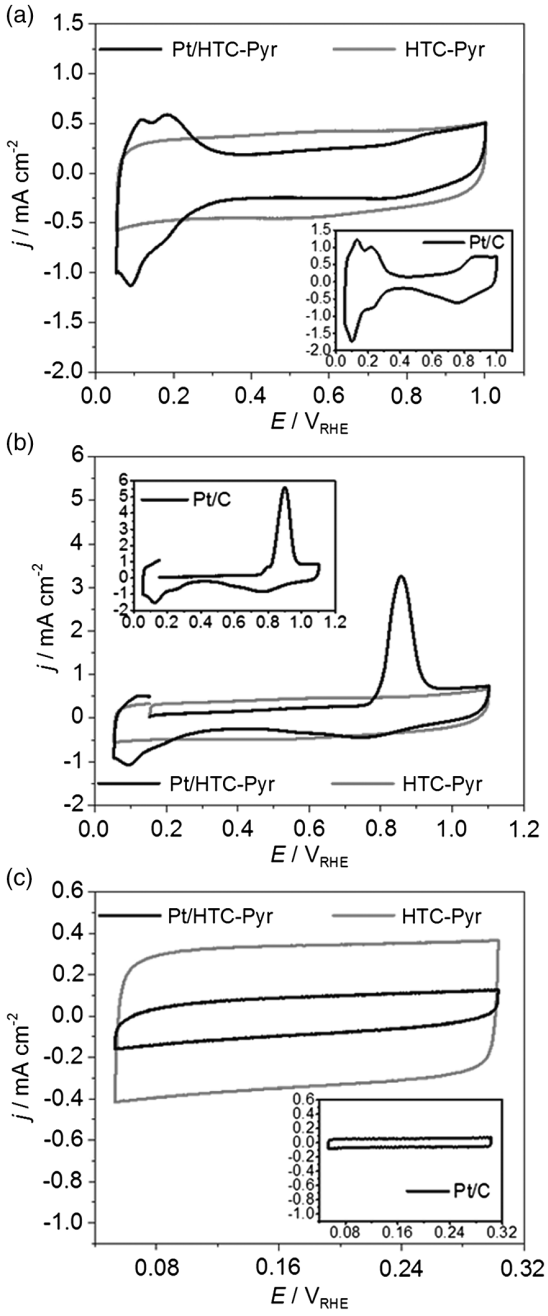

Figure 7. a,b) Cyclic and CO stripping voltammetry curves and c) cyclic voltammetry curves with adsorbed CO of Pt on pyrolyzed hydrochar (Pt/HTC-Pyr) and only HTC-Pyr in comparison with commercial Pt/C.[52]

species is visible at around 0.6 V_{RHE}. This is also reported for other carbons derived from hydrothermal carbonization.[26]

$$\mathrm{ECSA} = \frac{Q_{Pt}}{\upsilon \cdot \rho \cdot m_{Pt}} \quad (2)$$

CO stripping experiments are shown in Figure 7b. The curve of Pt/HTC-Pyr shows the CO oxidation in terms of a symmetric signal at 0.86 V_{RHE}. Several Pt catalysts based on the carbon

supports show a rather asymmetric CO oxidation peak in terms of an overlapping peak at a lower potential, which is reported to appear due to a lowered onset potential of CO oxidation on Pt particle aggregates instead of isolated single particles.[62–64] The absence of this asymmetry in CO stripping indicates the absence of Pt aggregates, which is in line with the well-distributed Pt particles seen in Figure 4c. In comparison, Pt/C shows the CO oxidation centered at 0.90 V_{RHE} with a small peak shoulder at the lower potential side. This indicates the presence of Pt aggregates in Pt/C.[62–64]

The ECSAs are calculated using Equation (2) with a charge density ρ of 4.2 C m_{Pt}^{-2} in case of CO adsorption on platinum. While during HUPD the hydrogen atom is adsorbed on one platinum atom, the CO stripping involves two platinum atoms. The CO molecule is supposed to be adsorbed on one platinum atom and to be oxidized through an oxygen species being adsorbed on another platinum atom.[65,66] Thus, the charge density is twice compared with HUPD. ECSA of Pt/HTC-C counts 83 m^2 g_{Pt}^{-1}, so that the average of ECSA from HUPD and from CO is 69 ± 21 m^2 g_{Pt}^{-1}. This is highly similar to commercial Pt/C[52] possessing an averaged ECSA determined by same methods and same experimental setups of 69 ± 6 m^2 g_{Pt}^{-1}.

Figure 7c shows CV curves in the regime of 0.05–0.30 V_{RHE} during CO adsorption onto the Pt surface. Thereby, the capacitive currents are recorded without interfering Faradaic currents and serve for the calculation of the double-layer capacitance C_{DL} by Equation (3). The anodic current I_a and the cathodic current I_c at 0.16, 0.21, and 0.26 V_{RHE}, respectively, and the scan rate υ is used for calculation. CV of Pt/HTC-Pyr shows a lower capacitive current than the CV of Pt/C. In consequence, Pt/HTC-Pyr exhibits a capacitance of 1.7 mF cm^{-2}, which is higher than the capacitance of Pt/C[52] counting 1.2 mF cm^{-2}. The specific surface area of the electrode and support materials is known to highly impact the double-layer capacitance.[67] Herein, the specific surface area of HTC-Pyr is more than twice as high as the area of C as compared in Table 1. Next to the catalyst, only HTC-Pyr is electrochemically investigated as well. The CV curve is depicted in Figure 7c and exhibits a much larger capacitive current density than the related Pt catalyst. In consequence, HTC-Pyr has a four times higher double-layer capacitance of 6.7 mF cm^{-2} compared with Pt/HTC-Pyr with 1.7 mF cm^{-2}, so that the incorporation of Pt particles into HTC-Pyr leads to the reduction of C_{DL}. This might be due to the lowered mass fraction of HTC-Pyr within the catalyst or additionally due to the closed pores by the platinum nanoparticles. The same observation was done in the work of Taleb et al.[26] with a decreased capacitance by 30% due to the platinum deposition on their HTC-derived carbon.

$$C_{DL} = \frac{(I_c - I_a)}{2 \cdot \upsilon} \tag{3}$$

ORR curves from rotating disk electrode (RDE) experiments are shown in **Figure 8**a. Although Pt/HTC-Pyr and Pt/C curves are recorded at different rotation speeds, the RDE experiment of HTC-Pyr without Pt is restricted to 1600 rpm due to the negligible activity for ORR. For the Pt/HTC-Pyr catalyst, the onset of oxygen reduction is at 0.94 V_{RHE}. In other studies, a Pt catalyst using a support originated from pyrolysis of orange peels showed a lower ORR onset of 0.84 V_{RHE}[41] and a Pt catalyst using a support derived from HTC of D-glucose showed an onset in similar range of 0.90–0.95 V_{RHE} in agreement with our study.[26] However, we obtained the catalyst from coconut shells with a more complex chemical composition and complex reaction pathways during HTC than the single compound D-glucose from the other study.[26] The commercial Pt/C[52] possesses a larger ORR onset potential of 1.00 V_{RHE} compared with Pt/HTC-Pyr.

$$j_{kin} = \frac{j_{lim} \cdot j}{j_{lim} - j} \tag{4}$$

Next to consideration of the ORR onset, the RDE experiments are used to determine the catalytic activity for oxygen reduction and to calculate the kinetic current density j_{kin} at 1600 rpm and 0.8 V_{RHE} of cathodic scans. Equation (4) includes the diffusion-limited current density j_{lim} and the experimentally measured current density j. The mass activity is obtained by normalization of j_{kin} to the mass of platinum evaluated by ICP-MS, and the specific activity is determined by normalization of j_{kin} to ECSA evaluated by HUPD.

Table 2 shows that Pt/HTC-Pyr has a mass activity of 5.5 A g_{Pt}^{-1} and a specific activity of 0.010 mA cm^{-2}. The commercial Pt/C[52] in comparison shows a mass activity of 112.8 A g_{Pt}^{-1} and a specific activity of 0.172 mA cm^{-2}. Although the ECSAs of Pt/HTC-Pyr

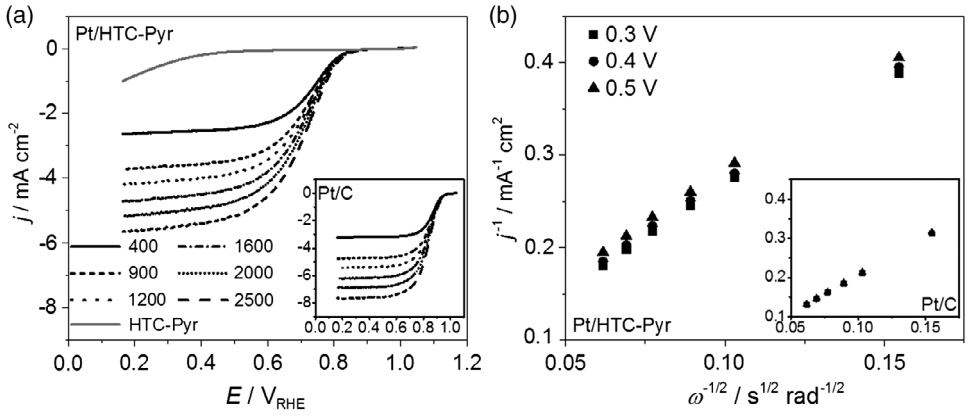

Figure 8. a) ORR curves of Pt/HTC-Pyr at different rotation speeds (400, 900, 1200, 1600, 2000, and 2500 rpm) and of only HTC-Pyr at 1600 rpm compared with ORR curves of commercial Pt/C[52]; b) Koutecky–Levich plot from ORR data of Pt/HTC-Pyr compared with commercial Pt/C[52].

Table 2. Parameters from the electrochemical analysis for Pt/HTC-Pyr and commercial Pt/C.[52]

Parameters	Pt/HTC-Pyr	Pt/C[52]
ECSA via HUPD [$m^2\,g_{Pt}^{-1}$]	54	65
ECSA via CO [$m^2\,g_{Pt}^{-1}$]	83	73
C_{DL} [mF cm^{-2}]	1.7	1.2
ORR onset potential [V]	0.94	1.00
Number of electrons in ORR	3.8	4.4
Mass activity [$A\,g_{Pt}^{-1}$]	5.5	112.8
Specific activity [mA cm^{-2}]	0.010	0.172
Δ (ECSA averaged) [%]	−67	−31
Δ (ORR onset potential) [%]	−10	−4

and Pt/C discussed before are highly comparable, the catalytic activity for O_2 reduction strongly deviates. This difference usually results from differences in Pt nanoparticles in view of size, morphology, and distribution on the support.[55,68,69] However, this is not expected for this study, because the Pt nanoparticles on both supports HTC-Pyr and carbon black[52] are highly comparable, evidenced by TEM analysis. This is additionally proven by the similar ECSAs. Because Pt particle characteristics and experimental RDE details are similar and excluded as main cause, the carbon support and Pt–support interaction might impact the ORR activity. This impact is frequently discussed in the literature.[37,70,71] Recapitulating the physical difference of the HTC-Pyr and carbon analyzed before, HTC-Pyr has lower surface functionalities shown by XPS, a lower electrical conductivity, and a lower degree of graphitization shown by XRD than Vulcan, which can affect anchoring of Pt nanoparticles and thus the Pt–support interaction. In consequence, charge transfers during ORR[72] and thus the rate-determining steps of ORR catalysis can be adversely affected. Regarding O_2 reduction in the acidic media, this involves, after dissociative oxygen adsorption on Pt's surface, an electron transfer to form adsorbed hydroxides followed by an electron transfer to form H_2O. The associative mechanism consists of O_2 adsorption on Pt and a first rate-determining step of electron transfer to form peroxo intermediates and later hydroxides and water.[72,73]

At potentials below ≈0.6 V_{RHE}, the current density is limited by oxygen diffusion and in consequence depends on the applied rotation speed of the RDE. This dependency is used for Koutecky–Levich (K–L) evaluation in Figure 8b and is used to determine the number of transferred electrons during O_2 reduction as described in Equation (5). n is the number of transferred electrons per O_2 molecule, F the Faraday constant (96 485 C mol^{-1}), θ the kinematic viscosity of the electrolyte (0.01 $cm^2\,s^{-1}$),[74] D the O_2 diffusion coefficient (1.93×10^{-5} $cm^2\,s^{-1}$),[74] c^* the concentration of oxygen in solution (1.26×10^{-3} mol L^{-1}),[74] and ω the rotation rate. The number of electrons is 3.8 in case of Pt/HTC-Pyr and 4.4 in case of Pt/C,[52] which is caused by a reaction involving four electrons and which is known as direct ORR mechanism on Pt catalysts.[72,75]

$$\frac{1}{j} = \frac{1}{j_{kin}} + \frac{1}{j_{lim}} = \frac{1}{0.62 \cdot n \cdot F \cdot \theta^{-1/6} \cdot D^{2/3} \cdot c^*} \cdot \omega^{-1/2} \quad (5)$$

Furthermore, an electrochemical stress test is performed to provoke catalyst degradation and to assess the stability. **Figure 9** depicts the results for Pt/HTC-Pyr compared with Pt/C. Figure 9a shows the CV curves before and after stress testing. The double-layer region between 0.35–0.70 V_{RHE} has significantly changed for Pt/HTC-Pyr in terms of an enlarged HQ/Q redox activity and an enlarged double layer capacitance, while changes in Pt/C[52] are negligible. This shows higher degradation of the carbon support derived from HTC than degradation of Vulcan. The lower degree of graphitization determined by XRD and the larger surface area of HTC-Pyr compared with Vulcan is supposed to affect the carbon stability.[76–78] Furthermore, signal intensities of hydrogen and oxygen reactions are decreased for both catalysts. ECSA of Pt/HTC-Pyr calculated by HUPD changed from 54 to 19 $m^2\,g_{Pt}^{-1}$, whereas the ECSA of standard Pt/C[52] changed from 65 to 48 $m^2\,g_{Pt}^{-1}$.

Figure 9b illustrates changes in the CO stripping curves. Signal intensities of CO oxidation decreased, which also shows the degradation of both catalysts. Pt/HTC-Pyr additionally shows an altered peak position and shape of CO oxidation. The signal is shifted from 0.86 to 0.88 V_{RHE} and consists of two overlapping peaks after the stress test, so that platinum nanoparticles might have changed to different Pt surfaces for CO adsorption and oxidation.[65] In contrast, degradation of standard Pt/C[52] results in same peak position and shape. ECSA of Pt/HTC-Pyr calculated by CO stripping decreased from 83 to 27 $m^2\,g_{Pt}^{-1}$, while the ECSA of Pt/C[52] decreased from 73 to 48 $m^2\,g_{Pt}^{-1}$. The averaged ECSA losses are compared in Table 2 and count −67% for Pt/HTC-Pyr and −31% for Pt/C. This higher ECSA loss and thus stronger degradation of Pt on HTC-Pyr are assumed to be the consequence of a significant larger HTC-Pyr instability compared with Vulcan. Stronger support degradation leads to stronger Pt degradation and thus loss of ECSA. Furthermore, XPS in Figure 6 reveals lower surface functionalities of the HTC-derived carbon, so that Pt nanoparticles might be less stabilized and underlie stronger degradation.

Figure 9c shows the cyclic voltammetry curves during CO adsorption and reveals an increased capacitive current density in case of Pt/HTC-Pyr and an almost unchanged capacitive current density for Pt/C.[52] For Pt/HTC-Pyr, the double-layer capacitance is enlarged by +208%. Electrode porosity and hydrophilicity evidently increased through carbon corrosion and impact C_{DL}.[67,79] Figure 9d compares the shifts of ORR curves after stress testing. The curve of Pt/HTC-Pyr underlies a stronger shift to lower potentials than the curve of Pt/C.[52] Table 2 shows the change of onset potential for ORR being −4% for standard Pt/C[52] and −10% for Pt/HTC-Pyr. Thus, oxygen reduction is more affected in case of Pt/HTC-Pyr, which is caused by stronger carbon support degradation and a higher loss of ECSA. In consequence, the stronger corrosion of carbon based on HTC, in this study, leads to higher Pt catalyst degradation compared with the commercial Pt/C.

3. Conclusions

A sustainable Pt catalyst support derived via HTC from coconut shells, a real biomass with highly complex chemical composition is investigated on the ORR in acidic environment. The char

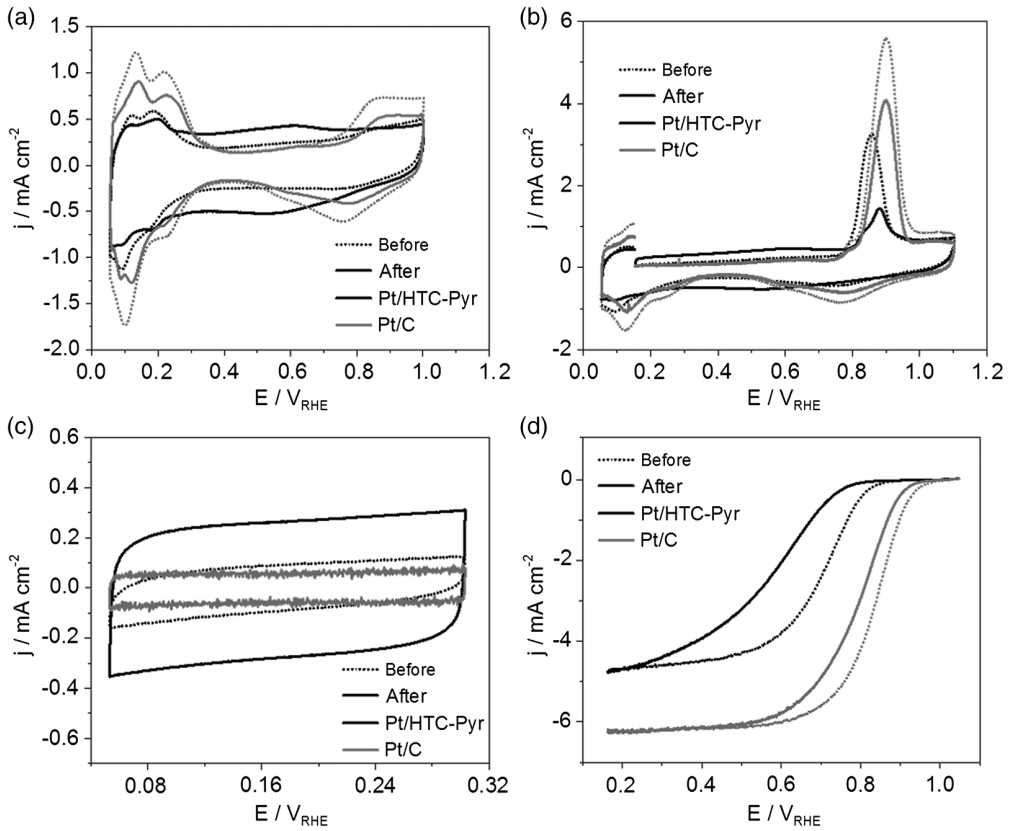

Figure 9. Comparison of a) cyclic and b) CO stripping voltammetry curves, of c) cyclic voltammetry curves with adsorbed CO and of d) ORR curves at a rotation speed of 1600 rpm before and after stress test for Pt/HTC-Pyr and Pt/C[52].

activation by pyrolysis resulted in a carbon support that best meets the requirements of sufficient porosity and electrical conductivity. The activated carbon possessed a specific surface area 2.5 times higher and a double-layer capacitance 29% larger than the commonly used Vulcan. Thereby, a high distribution of Pt particles on its surface was promoted and gave an ECSA of 69 $m^2 g_{Pt}^{-1}$ in the range of PEMFC catalysts.[52]

However, this carbon from HTC showed in XRD a much lower degree of graphitization than Vulcan and in consequence a two times lower electrical conductivity. Catalytic ORR activity of the Pt catalyst based on HTC was also lower and is believed to be caused by the support characteristics, since the Pt particle characteristics and distribution on the support surface was highly comparable with the commercial Pt catalyst. The more amorphous structure of the HTC-derived carbon might affect the Pt–support interaction and increase barriers for charge transfers. This might impact the kinetics of reaction steps such as electron transfers during oxygen reduction.

Nevertheless, this study proves the application of HTC in the synthesis of PEMFC catalyst supports derived from waste biomasses and presents the basis and understanding for further catalyst development by HTC and/or pyrolysis of chemically highly complex waste biomasses. The few other studies linking HTC and PEMFC application used much more simple chemical compounds such as saccharides,[26,42] whereas coconut shells contain large fractions of lignin compounds next to cellulose. More studies are required to evaluate the impact of the lignin content in the biomass.

Further optimization of biomass-derived catalyst supports could be in terms of increasing the electrical conductivity and the degree of graphitization, both factors being suggested to promote the ORR catalysis. First, thermal treatment of hydrochar at higher temperature than 1100 °C can enlarge the aromatic arrays and to enhance the graphitization.[39] After pyrolysis at higher temperatures, it might be necessary to oxidatively treat the surface by, e.g., boiling in HNO_3[37] to regenerate defect sites for strengthened Pt anchoring.

4. Experimental Section

All chemicals were used as received: coconut shell powder (COCONIT 300, Mahlwerk Neubauer-Friedrich Geffers GmbH, Germany), zinc chloride (anhydrous, 98%, Alfa Aesar GmbH & Co KG, Germany), potassium hydroxide (85%, Carl Roth GmbH und Co. KG, Germany), hydrochloric acid (37%, Carl Roth GmbH und Co. KG, Germany), chloroplatinic acid (Thermo Fisher GmbH, Germany), ethylene glycol (Carl Roth GmbH und Co. KG, Germany) ,and perchloric acid (70 wt%, Sigma-Aldrich Corporation, USA).

Activated carbons were prepared in two steps: HTC of coconut shell powder in a zinc chloride solution and subsequent activation of the hydrochar. HTC was carried out in 60 wt% aqueous zinc chloride for 12 h at 180 °C in a 2 L stainless steel autoclave with polytetrafluoroethylene (PTFE) inlet (BR-2000, Berghof). The autoclave was filled to three quarters with a ratio of saline to biomass of 1:2. The temperature was regulated via

a heating mantle and controlled with an external temperature controller. An initial pressure of 2 bar was set with compressed air. After 12 h, the autoclave was cooled down to room temperature. The hydrochar was separated from process water by vacuum filtration, washed with 1 L of deionized water and dried overnight at 105 °C. Later, the obtained hydrochar was activated using three different methods. The first method was named physical activation ("Phys") and took place in a tube furnace for 1 h at 650 °C in nitrogen atmosphere. Hydrochar (1 g) was put into a ceramic crucible and was placed into the furnace. A temperature controller was connected to a PT100 thermo element, which measured the temperature in the middle of the furnace. A round flask at the bottom contained the evaporating liquid in terms of deionized water, so that the steam was in contact with the hydrochar. After 1 h, the furnace was cooled down to 100 °C. The activated carbon was washed with 250 mL of deionized water and dried overnight at 75 °C. The second method named chemical activation ("Chem") took place in an analogous way, whereby the round flask at the bottom contained evaporating 1 mol L^{-1} aqueous KOH. After cooling down the furnace to 100 °C, the activated carbon was washed with 250 mL 0.1 mol L^{-1} aqueous HCl and dried overnight at 75 °C. The third method was called thermal activation via pyrolysis ("Pyr") of the hydrochar at 1100 °C for 2 h in an argon atmosphere with 5 vol% of hydrogen followed by ball milling for 1 min at 250 rpm. Next to these activated carbons, commercial Vulcan XC72R (Cabot Corporation, Malaysia) was considered as the reference material.

For the synthesis of platinum nanoparticles, 725 mg of chloroplatinic acid hexahydrate was put into 88 mL ethylene glycol. Aqueous NaOH (12 mL of 2 mol L^{-1}) was added to adjust pH 12. The solution was stirred for 4 h at 140 °C to obtain the platinum nanoparticles. Then, the Pt catalyst was prepared by centrifuging 1.6 mL of the suspension three times in 1 mol L^{-1} aqueous hydrochloric acid followed by deionized water. The centrifuged Pt nanoparticles and 16 mg of activated carbon were united in acetone and sonicated, until the solvent was evaporated. The final catalyst was washed with deionized water and dried at 60 °C under vacuum for 48 h. Next to the obtained Pt catalyst derived from HTC, commercial Pt on Vulcan XC72 (Sigma Aldrich Corporation, USA) was used as the reference and analyzed in the previous study.[52]

TGA was carried out using TGA 4000 (Perkin Elmer Corporation, USA) consisting of the furnace with balance, Al_2O_3 crucible, temperature sensor, heating/cooling elements, and the Pyris software for data recording. Before measurements, nitrogen purging for 30 min with 40 mL min^{-1} was done and the crucible was baked out. TGA was carried out in nitrogen atmosphere. The temperature program was: 3 min at 30, 30 to 100 °C at 10 °C min^{-1}, 10 min at 100, 100 to 900 °C at 10 °C min^{-1}, and finally 1 min at 900 °C. IR spectroscopy was carried out using Spectrum 100 Optica (Perkin Elmer Corporation, USA) consisting of a ZnSe crystal for ATR and the Spectrum software. After recording the background, the sample was measured using ten scans with a resolution of 4 cm^{-1}. Nitrogen sorption was carried out at 77 K with the TRISTAR II 3020 (Micromeritics GmbH, Germany) followed by BET analysis.[66] Before measurement, the samples were dried overnight under vacuum at 150 °C. Then, data of adsorption and desorption were collected over a pressure range of $p/p_0 = 0.005$–0.95 (36 points, randomly chosen by the measurement mode) and $p/p_0 = 0.95$–0.1 (19 points, linear distribution), respectively. The free space was measured with helium. Specific surface areas were calculated using the BET model in accordance with the Rouquerol criteria.[67] Apart from the calculation of the surface area, the distribution of pore sizes was determined. For this, the method based on the computational quantum mechanical modeling density functional theory (DFT) can be used, which is independent of capillary condensation and can therefore be applied over the whole micro- and mesopore range. Here, the nonlocal density functional theory (NLDFT) model for slit pores was used applying smoothing approximations to the DFT and the MicroActive Interactive Data Analysis Software. Electrical sheet resistances were measured via the four-point probe method using RM3-AR (Jandel Engineering Ltd, UK). A suspension analogous to the electrode preparation for electrochemical measurements below was prepared. A thin film was sprayed onto a glass substrate using a devilbiss spray gun (Carlisle Fluid Technologies Germany GmbH, Germany) operated with nitrogen. Five positions on each thin film were measured and averaged.

TEM was carried out using EM 902A (Carl Zeiss AG, Germany) with tungsten wire, an acceleration voltage of 80 kV, CCD sensor and iTEM Five software. Samples were suspended in ethanol and dropped onto polyvinyl formal coated copper grids with 200 meshes (Plano GmbH, Germany). 300 Pt nanoparticle diameters were determined and averaged by the software ImageJ. ICP-MS was carried out using XSeries2 (Thermo Fisher Scientific GmbH, Germany) to determine and average the Pt concentration of the isotopes ^{194}Pt, ^{195}Pt, and ^{196}Pt. 2.0 mg of the catalyst was digested overnight in 1.6 mL hydrochloric acid and 1.2 mL HNO_3. The digestion was filtered, diluted to 250 mL, and further diluted by factor of 5. Pt calibration solutions (100, 200, 400, 600, and 800 µg L^{-1}) were prepared on basis of the 1000 mg L^{-1} ICP standard solution (Carl Roth GmbH & Co. KG, Germany). Lutetium in a concentration of 1 mg L^{-1} was used as internal standard. XRD was carried out by the EMPYREAN Series 2 (PANalytical B.V., the Netherlands) using Cu Kα radiation, gonio scans with 2θ steps of 0.01° and DataCollector software. Patterns were evaluated by the HighScorePlus software and compared with patterns from the ICSD (FIZ Karlsruhe GmbH, Germany). Interplanar atomic distances d were determined by Bragg's law. XPS was performed using ESCALAB 250 Xi (Thermo Fisher, UK) and Al Kα radiation. To record the survey scans, a pass energy of 100 eV, a dwell time of 20 ms, and an energy step size of 1 eV were chosen. In each measurement, five scans were averaged. For high-resolution scanning of C1s and O1s regions, a pass energy of 10 eV, a dwell time of 50 ms, and an energy step size of 0.02 eV were selected. Also five scans were averaged. Background correction and peak fitting for analysis of the spectra were carried using Advantage (v.5.932, Thermo Fisher, UK) and using Gauss–Lorentz line shape and Smart background correction.

For electrochemical measurements, RDEs with glassy carbon showing an electrode area of 0.2 cm^2 and PTFE jacket were coated with catalyst or support samples and used as the working electrode inside an electrochemical half-cell. RDEs were polished 5 min each using pastes of alumina particles with diameters of 5.00 and 0.05 µm (Buehler, USA) followed by sonication in 2-propanol and in water for 5 min each. After drying the electrodes, catalyst or support thin films onto the RDEs were prepared. The inks contained 2-propanol and deionized water in a ratio of 1/3 with 2 g L^{-1} catalyst and 1.2 µg L^{-1} Nafion (registered trademark) and were sonicated for 1 h. After that, 14.7 µL of the ink was put on the electrode and dried at 700 rpm. The loading of catalyst or support thin films onto the working electrode counted to 150 µg cm^{-2} with a Pt loading of 12.4 µg cm^{-2} in case of the catalyst. Electrochemical measurements were carried out using the PGSTAT132N bipotentiostat (Metrohm Autolab, the Netherlands) controlled by the Nova 1.11 software and a three-electrode setup with the RDE as working electrode, Pt wire as counter electrode, and saturated calomel (SCE, KCl-sat.) as the reference electrode in 0.1 mol L^{-1} aqueous $HClO_4$ at room temperature. Electrochemical data were converted to the reversible hydrogen electrode (RHE). First, a potential cycling activation (100 cycles, 0.05–1.47 V_{RHE}, 500 mV s^{-1}, N_2-sat.) was carried out. Second, CV was performed (three cycles, 0.05–1.00 V_{RHE}, 50 mV s^{-1}, N_2-sat.) to analyze the ECSA from hydrogen underpotential deposition (HUPD). Also, CO stripping voltammetry was performed to analyze the ECSA. Therefore, a potential of 0.15 V_{RHE} was held and CO was bubbled for 1 min through the electrolyte followed by N_2 bubbling for 20 min. CV was done (three cycles, 0.05–0.30 V_{RHE}, 50 mV s^{-1}, N_2-sat.) to control complete CO adsorption on Pt. Finally, the stripping voltammetry was carried out by starting the anodic scan from 0.15 V_{RHE} (3 cycles, 0.15–1.10 V_{RHE}, 50 mV s^{-1}, N_2-sat.). For recording ORR curves, CV was used (three cycles, 0.16–1.05 V_{RHE}, 5 mV s^{-1}, O_2-sat.) during rotation of the RDE at 400, 900, 1200, 1600, 2000, and 2500 rpm each. Last, an electrochemical stress test induced catalyst degradation to evaluate the stability of Pt/HTC-Pyr and Pt/C. Triangle-waved potential cycling was carried out between 0.05 and 1.47 V_{RHE} in O_2-saturated electrolyte with 1000 cycles and a scan rate of 500 mV s^{-1}.

Acknowledgements

The funding by the German Federal Ministry for Economic Affairs in the framework of the project "QUALIFIX" (03ET6046A) as well as by the EU-Interreg V-A project "Groene Kaskade" (151073) is greatly appreciated. The authors thank Julia Hülstede for the support in experimental work.

Conflict of Interest

The authors declare no conflict of interest.

Keywords

biomasses, fuel cells, oxygen reduction reactions, platinum, supported catalysts

Received: March 25, 2019
Revised: July 18, 2019
Published online:

[1] P. Gerland, A. E. Raftery, H. Ševčíková, N. Li, D. Gu, T. Spoorenberg, L. Alkema, B. K. Fosdick, J. Chunn, N. Lalic, G. Bay, T. Buettner, G. K. Heilig, J. Wilmoth, *Science* **2014**, *346*, 234.
[2] G. Marland, T. A. Boden, R. J. Andres, *Global, Regional, and National Fossil-Fuel CO_2 Emissions*, Carbon Dioxide Information Analysis Center, Oak Ridge National Laboratory, U.S. Department of Energy, Oak Ridge, Tenn., USA **2017**.
[3] United Nations, presented at *United Nations Climate Change Conf.*, Paris, France **2015**, p. 1.
[4] M.-M. Titirici, A. Thomas, M. Antonietti, *New J. Chem.* **2007**, *31*, 787.
[5] S. Schimmelpfennig, C. Müller, L. Grünhage, C. Koch, C. Kammann, *Agric., Ecosyst. Environ.* **2014**, *191*, 39.
[6] J. A. Ippolito, D. A. Laird, W. J. Busscher, *J. Environ. Qual.* **2012**, *41*, 967.
[7] Y. Q. Lei, H. Q. Su, *Adv. Mater. Res.* **2013**, *726–731*, 634.
[8] J. Fang, B. Gao, J. Chen, A. R. Zimmerman, *Chem. Eng. J.* **2015**, *267*, 253.
[9] A. Kruse, A. Funke, M.-M. Titirici, *Curr. Opin. Chem. Biol.* **2013**, *17*, 515.
[10] J. A. Libra, K. S. Ro, C. Kammann, A. Funke, N. D. Berge, Y. Neubauer, M.-M. Titirici, C. Fühner, O. Bens, J. Kern, K.-H. Emmerich, *Biofuels* **2011**, *2*, 71.
[11] B. V. Babu, *Biofuels, Bioprod. Biorefin.* **2008**, *2*, 393.
[12] O. Ioannidou, C. G. Jung, A. Zabaniotou, *Catal. Today* **2011**, *167*, 129.
[13] M. K. Akalın, K. Tekin, S. Karagöz, *Bioresour. Technol.* **2012**, *110*, 682.
[14] J. Akhtar, N. A. S. Amin, *Renewable Sustainable Energy Rev.* **2011**, *15*, 1615.
[15] K. Anastasakis, A. B. Ross, *Bioresour. Technol.* **2011**, *102*, 4876.
[16] B. Ibrahim, M. Schlegel, N. Kanswohl, *Appl. Agric. Forestry Res.* **2014**, *64*, 119.
[17] D. Kim, K. Yoshikawa, K. Y. Park, *Energies* **2015**, *8*, 12412.
[18] A. Funke, F. Ziegler, *Biofuels, Bioprod. Biorefin.* **2010**, *4*, 160.
[19] A. Jain, R. Balasubramanian, M. P. Srinivasan, *Chem. Eng. J.* **2016**, *283*, 789.
[20] M.-M. Titirici, M. Antonietti, *Chem. Soc. Rev.* **2010**, *39*, 103.
[21] A. Spataru, R. Jain, J. W. Chung, G. Gerner, R. Krebs, P. N. L. Lens, *RSC Adv.* **2016**, *6*, 101827.
[22] M. Sevilla, W. Sangchoom, N. Balahmar, A. B. Fuertes, R. Mokaya, *ACS Sustain. Chem. Eng.* **2016**, *4*, 4710.
[23] W. Lu, S. Marta, A. B. Fuertes, M. Robert, Y. Gleb, *Adv. Energy Mater.* **2011**, *1*, 356.
[24] L. Wei, M. Sevilla, A. B. Fuertes, R. Mokaya, G. Yushin, *Adv. Energy Mater.* **2011**, *1*, 356.
[25] S.-A. Wohlgemuth, R. J. White, M.-G. Willinger, M.-M. Titirici, M. Antonietti, *Green Chem.* **2012**, *14*, 1515.
[26] M. Taleb, J. Nerut, T. Tooming, T. Thomberg, A. Jänes, E. Lust, *J. Electrochem. Soc.* **2015**, *162*, F651.
[27] B. Ledesma, M. Olivares-Marín, A. Álvarez-Murillo, S. Roman, J. M. V. Nabais, *J. Supercrit. Fluids* **2018**, *138*, 187.
[28] L. Ding, B. Zou, Y. Li, H. Liu, Z. Wang, C. Zhao, Y. Su, Y. Guo, *Colloids Surf., A* **2013**, *423*, 104.
[29] A. Jain, R. Balasubramanian, M. P. Srinivasan, *Chem. Eng. J.* **2015**, *273*, 622.
[30] H. N. Tran, S.-J. You, H.-P. Chao, *J. Environ. Manage.* **2017**, *188*, 322.
[31] S. Román, J. M. Valente Nabais, B. Ledesma, J. F. González, C. Laginhas, M. M. Titirici, *Microporous Mesoporous Mater.* **2013**, *165*, 127.
[32] M. Sevilla, G. A. Ferrero, A. B. Fuertes, *Carbon* **2017**, *114*, 50.
[33] L. Zhu, F. Shen, R. L. Smith, Jr., X. Qi, *Energy Technol.* **2017**, *5*, 452.
[34] M. A. Islam, M. J. Ahmed, W. A. Khanday, M. Asif, B. H. Hameed, *Ecotoxicol. Environ. Saf.* **2017**, *138*, 279.
[35] K. Takeuchi, M. Fujishige, N. Ishida, Y. Kunieda, Y. Kato, Y. Tanaka, T. Ochi, H. Shirotori, Y. Uzuhashi, S. Ito, K.-I. Oshida, M. Endo, *J. Phys. Chem. Solids* **2018**, *118*, 137.
[36] L. Wang, Y. Guo, B. Zou, C. Rong, X. Ma, Y. Qu, Y. Li, Z. Wang, *Bioresour. Technol.* **2011**, *102*, 1947.
[37] S. Samad, K. S. Loh, W. Y. Wong, T. K. Lee, J. Sunarso, S. T. Chong, W. R. W. Daud, *Int. J. Hydrogen Energy* **2018**, *43*, 7823.
[38] M. Liu, R. Zhang, W. Chen, *Chem. Rev.* **2014**, *114*, 5117.
[39] L. N. Cleemann, F. Buazar, Q. Li, J. O. Jensen, C. Pan, T. Steenberg, S. Dai, N. J. Bjerrum, *Fuel Cells* **2013**, *13*, 822.
[40] K.-S. Lee, I.-S. Park, Y.-H. Cho, D.-S. Jung, N. Jung, H.-Y. Park, Y.-E. Sung, *J. Catal.* **2008**, *258*, 143.
[41] M. Dhelipan, A. Arunchander, A. Sahu, D. Kalpana, *J. Saudi Chem. Soc.* **2017**, *21*, 487.
[42] M. Sevilla, C. Sanchís, T. Valdés-Solís, E. Morallón, A. B. Fuertes, *Electrochim. Acta* **2009**, *54*, 2234.
[43] Y. Wang, S. Zuo, Y. Liu, *Electrochim. Acta* **2018**, *263*, 465.
[44] M. Borghei, N. Laocharoen, E. Kibena-Põldsepp, L.-S. Johansson, J. Campbell, E. Kauppinen, K. Tammeveski, O. J. Rojas, *Appl. Catal., B* **2017**, *204*, 394.
[45] R. Alipour Moghadam Esfahani, L. Osmieri, S. Specchia, S. Yusup, A. Tavasoli, A. Zamaniyan, *Chem. Eng. J.* **2017**, *308*, 578.
[46] H. Schmidt, *PhD Thesis*, Universität Duisburg-Essen, Duisburg, Germany **2003**.
[47] X. Gao, J. Jang, S. Nagase, *J. Phys. Chem. C* **2010**, *114*, 832.
[48] S. Pei, H.-M. Cheng, *Carbon* **2012**, *50*, 3210.
[49] M. Thommes, K. Kaneko, V. Neimark Alexander, P. Olivier James, F. Rodriguez-Reinoso, J. Rouquerol, S. W. Sing Kenneth, *Pure Appl. Chem.* **2015**, *87*, 1051.
[50] T. Sobolyeva, *PhD Thesis*, Simon Fraser University, Burnaby, BC, Canada **2010**.
[51] H. Multhaupt, *PhD Thesis*, Carl von Ossietzky Universität Oldenburg **2018**.
[52] D. Schonvogel, J. Hülstede, P. Wagner, A. Dyck, C. Agert, M. Wark, *J. Electrochem. Soc.* **2018**, *165*, F3373.
[53] A. Bianco, H.-M. Cheng, T. Enoki, Y. Gogotsi, R. H. Hurt, N. Koratkar, T. Kyotani, M. Monthioux, C. R. Park, J. M. D. Tascon, J. Zhang, *Carbon* **2013**, *65*, 1.
[54] S. Mukerjee, *J. Appl. Electrochem.* **1990**, *20*, 537.
[55] M. Peuckert, T. Yoneda, R. A. D. Betta, M. Boudart, *J. Electrochem. Soc.* **1986**, *133*, 944.
[56] C. He, S. Desai, G. Brown, S. Bollepalli, *Electrochem. Soc. Interface* **2005**, *14*, 41.

[57] S. Ratso, I. Kruusenberg, M. Vikkisk, U. Joost, E. Shulga, I. Kink, T. Kallio, K. Tammeveski, *Carbon* **2014**, *73*, 361.
[58] Y. Shao, S. Zhang, C. Wang, Z. Nie, J. Liu, Y. Wang, Y. Lin, *J. Power Sources* **2010**, *195*, 4600.
[59] J. Ma, A. Habrioux, Y. Luo, G. Ramos-Sanchez, L. Calvillo, G. Granozzi, P. B. Balbuena, N. Alonso-Vante, *J. Mater. Chem. A* **2015**, *3*, 11891.
[60] L. Zhao, Z.-B. Wang, J.-L. Li, J.-J. Zhang, X.-L. Sui, L.-M. Zhang, *Electrochim. Acta* **2016**, *189*, 175.
[61] R. M. Darling, J. P. Meyers, *J. Electrochem. Soc.* **2003**, *150*, A1523.
[62] S. Taylor, E. Fabbri, P. Levecque, T. J. Schmidt, O. Conrad, *Electrocatalysis* **2016**, *7*, 287.
[63] K. Novikova, A. Kuriganova, I. Leontyev, E. Gerasimova, O. Maslova, A. Rakhmatullin, N. Smirnova, Y. Dobrovolsky, *Electrocatalysis* **2018**, *9*, 22.
[64] A. López-Cudero, J. Solla-Gullón, E. Herrero, A. Aldaz, J. M. Feliu, *J. Electroanal. Chem.* **2010**, *644*, 117.
[65] P. Urchaga, S. Baranton, C. Coutanceau, G. Jerkiewicz, *Langmuir* **2012**, *28*, 3658.
[66] T. Vidakovic, M. Christov, K. Sundmacher, *Electrochim. Acta* **2007**, *52*, 5606.
[67] M. J. Bleda-Martínez, J. A. Maciá-Agulló, D. Lozano-Castelló, E. Morallón, D. Cazorla-Amorós, A. Linares-Solano, *Carbon* **2005**, *43*, 2677.
[68] C. Wang, H. Daimon, T. Onodera, T. Koda, S. Sun, *Angew. Chem.* **2008**, *120*, 3644.
[69] K. Kinoshita, *J. Electrochem. Soc.* **1990**, *137*, 845.
[70] T. Kinumoto, N. Eguchi, M. Matsuoka, T. Tsumura, M. Toyoda, *ECS Trans.* **2013**, *50*, 1701.
[71] A. Bharti, G. Cheruvally, *J. Power Sources* **2017**, *360*, 196.
[72] J. K. Norskov, J. Rossmeisl, A. Logadottir, L. Lindqvist, J. R. Kitchin, T. Bligaard, H. Jónsson, *J. Phys. Chem. B* **2004**, *108*, 17886.
[73] N. Ramaswamy, S. Mukerjee, *Adv. Phys. Chem.* **2012**, *2012*, 491604.
[74] W. Sheng, S. W. Lee, E. J. Crumlin, S. Chen, Y. Shao-Horn, *J. Electrochem. Soc.* **2011**, *158*, B1398.
[75] I. Katsounaros, S. Cherevko, A. R. Zeradjanin, K. J. J. Mayrhofer, *Angew. Chem., Int. Ed.* **2014**, *53*, 102.
[76] S. C. Ball, S. L. Hudson, D. Thompsett, B. Theobald, *J. Power Sources* **2007**, *171*, 18.
[77] D. Stevens, M. Hicks, G. Haugen, J. Dahn, *J. Electrochem. Soc.* **2005**, *152*, A2309.
[78] C.-C. Hung, P.-Y. Lim, J.-R. Chen, H. C. Shih, *J. Power Sources* **2011**, *196*, 140.
[79] D. Lozano-Castelló, D. Cazorla-Amorós, A. Linares-Solano, S. Shiraishi, H. Kurihara, A. Oya, *Carbon* **2003**, *41*, 1765.
[80] D. Schonvogel, J. Hülstede, P. Wagner, I. Kruusenberg, K. Tammeveski, A. Dyck, C. Agert, M. Wark, *J. Electrochem. Soc.* **2017**, *164*, F995.
[81] D. Schonvogel, *PhD Thesis*, Carl von Ossietzky Universität Oldenburg, Oldenburg **2018**.